Space Vector Modulated Model Predictive Control applied to Four-Wire Inverters

Vítor Paese De Carli*, Hilton Abilio Grundling*, Humberto Pinheiro* and Rodrigo Varella Tambara*.
* Grupo de Eletrônica de Potência e Controle, Universidade Federal de Santa Maria - Santa Maria, Brazil

***Abstract*—This paper extends the Space Vector Modulated Model Predictive Control to three-phase four-wire inverters. By employing a discrete-time model in the $\alpha\beta 0$ frame with implementation delay, a continuous-control-set predictive controller is developed to ensure fixed switching frequency and high-bandwidth tracking. The optimization problem is solved analytically via Karush-Kuhn-Tucker conditions, ensuring real-time feasibility. Applied to a shunt active power filter under nonlinear and unbalanced loads, the strategy was validated through hardware-in-the-loop emulation. Results demonstrate precise current tracking, effective neutral current suppression, and stable DC-link regulation. Comparative analysis shows that SVM²PC outperforms conventional FCS-MPC in tracking error indices while achieving comparable harmonic mitigation, confirming its effectiveness for high-performance power quality applications.**

***Index Terms*—CCS-MPC, SAPF, Space Vector.**

I. Introduction

Model Predictive Control (MPC) has emerged as a powerful and flexible control strategy for power electronic systems, particularly in applications involving grid-connected converters and active power filters (APFs). Its ability to handle multiple constraints and optimize system performance in real-time makes it well-suited for controlling four-wire converters, which are often subjected to unbalanced loads and harmonic distortions. Recent advancements in MPC-based strategies have demonstrated significant improvements in power quality, efficiency, and dynamic response for such systems.

Several studies have investigated the use of MPC in different converter topologies. For example, [1] proposed an optimal switching sequence MPC for four-leg, two-level grid-connected converters, achieving fixed-frequency operation with low computational complexity. In a similar direction, [2] applied FCS-MPC to a three-level four-leg flying capacitor converter operating as a shunt active power filter (SAPF), reducing computational effort by decoupling capacitor voltage control from the cost function while also mitigating switch stress through a phase-to-phase control strategy. Applications to hybrid active power filters were explored in [3], where FCS-MPC was combined with adaptive notch filters and active damping loops to address resonance issues in dynamic reactive power compensation.

More recent works have focused on three-phase four-wire systems and specific application scenarios. In [4], FCS-MPC was applied to an SAPF in an off-grid micro-generation system, using instantaneous power theory to generate compensation references and allowing higher sampling frequencies. Predictive current control for a four-wire APF in metro railway systems was investigated in [5], employing a split-capacitor topology with dual control loops. Other contributions include modulated predictive current control for modular H-bridge-based APFs [6], neutral current elimination strategies in two-level H-bridge APFs [7], and reduced-complexity FCS-MPC schemes with predictive current and DC-link voltage control [8], which limit the number of tested voltage vectors without degrading performance.

This work extends the Space Vector Modulated Model Predictive Control (SVM²PC) strategy, originally introduced in [9], to four-wire inverters and applies it to a Shunt Active Power Filter (SAPF). The main contribution is the effective grid current harmonic mitigation, achieved by integrating the SVM²PC framework with p–q-based reference generation, Kalman filtering, positive-sequence extraction, and adaptive PID control for DC-link voltage regulation.

II. Discrete-time Model of Space Vector Modulated Four-Wire Inverter

The continuous-time dynamics of a three-phase, four-wire, two-level converter in the synchronous $\alpha\beta 0$ reference frame are governed by

$$\dot{\boldsymbol{x}} = \boldsymbol{A}\boldsymbol{x} + \boldsymbol{B}\boldsymbol{u} + \boldsymbol{F}\boldsymbol{\omega}, \tag{1}$$

where $\boldsymbol{x} \in \mathbb{R}^n$ is the state vector, $\boldsymbol{u}$ is the control input, and $\boldsymbol{\omega} \in \mathbb{R}^3$ is the disturbance vector. The control action is constrained to a finite set of 16 admissible switching vectors, defined as

$$\boldsymbol{\Omega} = \{\boldsymbol{v}^0, \boldsymbol{v}^1, \ldots, \boldsymbol{v}^{15}\}, \quad \boldsymbol{v}^i \in \mathbb{R}^3. \tag{2}$$

The Space Vector Modulation (SVM) synthesizes the average voltage vector by combining adjacent switching vectors over each sampling period. The admissible vector set forms a dodecahedron in the $\alpha\beta 0$ space, partitioned into 24 tetrahedral regions by six separation planes. Each tetrahedron comprises one zero and three adjacent nonzero vectors, ensuring low-distortion voltage synthesis.

Real-time sector identification is performed by evaluating the reference voltage position relative to the separation planes, defined as

$$\mathrm{SP}_i = \boldsymbol{n}_i \begin{bmatrix} u_\alpha & u_\beta & u_0 \end{bmatrix}^T = 0, \quad i = 1, \ldots, 6, \tag{3}$$

where $\boldsymbol{n}_i$ is the i-th normal vector.

Once the sector is identified, a symmetric seven-segment switching sequence is adopted for a two-level four-wire inverter, given by

$$\boldsymbol{s}_k = \{\boldsymbol{v}^0, \boldsymbol{v}^a, \boldsymbol{v}^b, \boldsymbol{v}^c, \boldsymbol{v}^b, \boldsymbol{v}^a, \boldsymbol{v}^0\}, \tag{4}$$

where $\boldsymbol{v}^0$ is the zero vector and $\boldsymbol{v}^a$, $\boldsymbol{v}^b$, and $\boldsymbol{v}^c$ are the nonzero vectors defining the selected tetrahedron. The corresponding dwell times are denoted by d_0, d_a, d_b, and d_c.

Assuming a constant switching sequence and disturbance over the sampling period T_s, the discrete-time state evolution can be expressed in compact form as

$$\boldsymbol{x}_{k+1} = \boldsymbol{A}_d \boldsymbol{x}_k + \boldsymbol{B}_d \begin{bmatrix} \boldsymbol{v}_k^a & \boldsymbol{v}_k^b & \boldsymbol{v}_k^c \end{bmatrix} \boldsymbol{d}_k + \boldsymbol{F}_d \boldsymbol{\omega}_k, \tag{5}$$

where $\boldsymbol{d}_k = \begin{bmatrix} d_k^a & d_k^b & d_k^c \end{bmatrix}^T$ collects the dwell times of the active vectors.

To account for the implementation delay inherent to digital control, an augmented discrete-time state-space model is adopted:

$$\begin{cases} \boldsymbol{z}_{k+1} = \boldsymbol{A}\boldsymbol{z}_k + \boldsymbol{B}\boldsymbol{u}_k + \boldsymbol{F}\boldsymbol{\omega}_k, \\ \quad \boldsymbol{y}_k = \boldsymbol{C}\boldsymbol{z}_k, \end{cases} \tag{6}$$

where $\boldsymbol{z}_k = \begin{bmatrix} \boldsymbol{x}_k^T & \boldsymbol{\phi}_k^T \end{bmatrix}^T$ includes the delay-related states $\boldsymbol{\phi}_k$. The control input is finally defined as

$$\boldsymbol{u}_k = \begin{bmatrix} \boldsymbol{v}_k^a & \boldsymbol{v}_k^b & \boldsymbol{v}_k^c \end{bmatrix} \boldsymbol{d}_k. \tag{7}$$

This augmented model and its associated control input constitute the basis for the formulation of the proposed SVM^{2}PC strategy, detailed in the following section.

III. Space Vector Modulated Model Predictive Control Applied to a Four-Wire Inverter

This section presents the development of an MPC strategy for a two-level three-phase four-wire converter, based on the discrete-time model given in (6). First, the associated optimization problem is formulated, and its solution is derived using the Karush–Kuhn–Tucker (KKT) conditions. In addition, a simplifying assumption is introduced to reduce the computational burden of the control law, making the approach suitable for real-time implementation.

A. Optimization Problem

Assuming a constant control input $\boldsymbol{u}_k$ over the prediction horizon N, the objective is to minimize the tracking error relative to the reference $\boldsymbol{r}_{k+N}$:

$$f = \|\boldsymbol{r}_{k+N} - \boldsymbol{y}_{k+N}\|^2. \tag{8}$$

By recursively applying the discrete-time model, the predicted state is expressed as

$$\boldsymbol{z}_{k+N} = \boldsymbol{A}^N \boldsymbol{z}_k + \left(\boldsymbol{A}^{N-1} + \cdots + \boldsymbol{A} + \boldsymbol{I}\right) \boldsymbol{B}\boldsymbol{u}_k + \bar{\boldsymbol{F}}\bar{\boldsymbol{\omega}}_k, \tag{9}$$

where the augmented disturbance vector $\bar{\boldsymbol{\omega}}_k$ and its corresponding matrix $\bar{\boldsymbol{F}}$ are defined as

$$\begin{aligned} \bar{\boldsymbol{\omega}}_k &= \begin{bmatrix} \boldsymbol{\omega}_k^T & \boldsymbol{\omega}_{k+1}^T & \dots & \boldsymbol{\omega}_{k+N-1}^T \end{bmatrix}^T, \\ \bar{\boldsymbol{F}} &= \begin{bmatrix} \boldsymbol{A}^{N-1}\boldsymbol{F} & \dots & \boldsymbol{A}\boldsymbol{F} & \boldsymbol{F} \end{bmatrix}. \end{aligned} \tag{10}$$

Substituting these expressions into the cost function yields the compact quadratic form

$$f = \|\boldsymbol{H}\boldsymbol{u} + \boldsymbol{h}\|^2, \tag{11}$$

with

$$\begin{aligned} \boldsymbol{H} &= -\boldsymbol{C}\left(\boldsymbol{A}^{N-1} + \cdots + \boldsymbol{A} + \boldsymbol{I}\right)\boldsymbol{B}, \\ \boldsymbol{h} &= \boldsymbol{r}_{k+N} - \boldsymbol{C}\boldsymbol{A}^N \boldsymbol{z}_k - \boldsymbol{C}\bar{\boldsymbol{F}}\bar{\boldsymbol{\omega}}_k. \end{aligned} \tag{12}$$

The resulting unconstrained optimization problem can be written as

$$\min_{\boldsymbol{u}\in\mathbb{R}^3} \ \|\boldsymbol{H}\boldsymbol{u} + \boldsymbol{h}_4\|^2. \tag{13}$$

However, in SVM, the control input is determined by the active tetrahedral region, resulting in region-specific state-space models. The cost function must therefore be reformulated for each tetrahedron i as

$$f = \|\boldsymbol{H}_i \boldsymbol{d} + \boldsymbol{h}\|^2, \tag{14}$$

where $\boldsymbol{H}_i = \begin{bmatrix} \boldsymbol{h}_1 & \boldsymbol{h}_2 & \boldsymbol{h}_3 \end{bmatrix}$, and

$$\begin{aligned} \boldsymbol{h}_1 &= -\boldsymbol{C}\left(\boldsymbol{A}^{N-1} + \cdots + \boldsymbol{A} + \boldsymbol{I}\right)\boldsymbol{B}\boldsymbol{v}_i^a, \\ \boldsymbol{h}_2 &= -\boldsymbol{C}\left(\boldsymbol{A}^{N-1} + \cdots + \boldsymbol{A} + \boldsymbol{I}\right)\boldsymbol{B}\boldsymbol{v}_i^b, \\ \boldsymbol{h}_3 &= -\boldsymbol{C}\left(\boldsymbol{A}^{N-1} + \cdots + \boldsymbol{A} + \boldsymbol{I}\right)\boldsymbol{B}\boldsymbol{v}_i^c. \end{aligned} \tag{15}$$

The optimization is also subject to duty-cycle constraints given by

$$\begin{aligned} g_1 &\coloneqq -1 + d_a + d_b + d_c \le 0, \\ g_2 &\coloneqq -d_a \le 0, \\ g_3 &\coloneqq -d_b \le 0, \\ g_4 &\coloneqq -d_c \le 0. \end{aligned} \tag{16}$$

Accordingly, the constrained optimization problem for the SVM^{2}PC strategy is formulated as

$$\begin{aligned} \min_{\boldsymbol{d}\in\mathbb{R}^3} \quad & \|\boldsymbol{H}_i\boldsymbol{d} + \boldsymbol{h}\|^2, \\ & i \in \{1, 2, \dots, 24\}, \\ \text{s.t.} \quad & g_1,\ g_2,\ g_3,\ g_4. \end{aligned} \tag{17}$$

B. Solution

Solving (17) for all 24 tetrahedra is computationally prohibitive for high-frequency power electronics. Instead, the SVM^{2}PC strategy employs two nested optimization steps: first, the unconstrained problem (13) is solved analytically to obtain $\boldsymbol{u}_{uc}^*$, identifying the active tetrahedral region. Assuming the constrained optimum lies within this same region, (17) is then solved locally. Notably, while the unconstrained formulation optimizes the synthesized voltage vector $\boldsymbol{u}$, the constrained step directly optimizes the duty-cycle vector $\boldsymbol{d}$ for the identified tetrahedron.

The solution of the unconstrained problem given by (13) is achieved by computing

$$\boldsymbol{u}_{uc}^* = -\left(\boldsymbol{H}^T\boldsymbol{H}\right)^{-1}\boldsymbol{H}^T\boldsymbol{h}_4. \tag{18}$$

Although $\boldsymbol{u}_{uc}^*$ is not guaranteed to lie inside the feasible region, its associated tetrahedron can be identified by evaluating the separation planes of the space vector diagram.

Once the i-th tetrahedron is identified, the constrained optimization problem defined in (17) is addressed. Under the initial assumption that no overmodulation occurs, the optimal duty cycle vector is obtained as

$$\boldsymbol{d}^{*} = -\left(\boldsymbol{H}_i^T \boldsymbol{H}_i\right)^{-1} \boldsymbol{H}_i^T \boldsymbol{h}. \tag{19}$$

If $\boldsymbol{d}^*$ satisfies the modulation constraints defined in (16), it is directly applied for the current sampling period. Otherwise, the converter enters overmodulation, and the optimal solution must lie on the boundary of the feasible region.

By applying the Karush-Kuhn-Tucker (KKT) conditions, the constrained solution for each valid active-set combination $j \in \{1, \ldots, 15\}$ is obtained by solving:

$$\begin{bmatrix} \boldsymbol{d}_j^* \\ \boldsymbol{\mu}_j \end{bmatrix} = \begin{bmatrix} 2\boldsymbol{H}_i^T \boldsymbol{H}_i & \nabla \boldsymbol{g}_j^T \\ \nabla \boldsymbol{g}_j & \boldsymbol{0} \end{bmatrix}^{-1} \begin{bmatrix} -2\boldsymbol{H}_i^T \boldsymbol{h} \\ \boldsymbol{k}_j \end{bmatrix}, \tag{20}$$

where $\nabla \boldsymbol{g}_j$ and $\boldsymbol{k}_j$ represent the Jacobian and the constant vector of the active constraints for case j, respectively.

For instance, when the modulation limit (g_1) and the non-negativity constraint for the first phase (g_2) are simultaneously active, the KKT stationarity condition is expressed as

$$\nabla f + \mu_1 \nabla g_1 + \mu_2 \nabla g_2 = \boldsymbol{0}. \tag{21}$$

The resulting system for the optimal feasible dwell times and multipliers is expanded as:

$$\begin{bmatrix} \boldsymbol{d}^* \\ \mu_1 \\ \mu_2 \end{bmatrix} = \begin{bmatrix} 2\boldsymbol{H}_i^T \boldsymbol{H}_i & \nabla g_1 & \nabla g_2 \\ \nabla g_1^T & 0 & 0 \\ \nabla g_2^T & 0 & 0 \end{bmatrix}^{-1} \begin{bmatrix} -2\boldsymbol{H}_i^T \boldsymbol{h} \\ 1 \\ 0 \end{bmatrix}, \tag{22}$$

where $\nabla g_1 = \begin{bmatrix} 1 & 1 & 1 \end{bmatrix}^T$, and $\nabla g_2 = \begin{bmatrix} -1 & 0 & 0 \end{bmatrix}^T$.

1) Remark: Although the KKT-based optimization may appear demanding, precomputing the analytical solutions for all 15 active-set cases shifts the primary computational burden offline. This strategy trades increased memory usage for minimal online execution time, ensuring real-time feasibility and optimal tracking during overmodulation with reasonable computational overhead.

IV. SVM^{2}PC Applied to Shunt-Active Power Filter

The proposed SVM^{2}PC strategy is evaluated through a case study on a SAPF. This section details the system modeling, control architecture, and implementation, focusing on the key design aspects and performance metrics under the proposed scheme. The system comprises a three-phase four-wire inverter connected to the grid via an L-type filter, as depicted in Fig. 1.

A. Modeling

Under the assumptions of a regulated DC-link voltage and ideal switching devices, the system in Fig. 1 is represented in the $\alpha\beta0$ frame as three decoupled single-phase subsystems, as shown in Fig. 2.

The primary control variables include the filter current $i_{f,x}$, the point-of-common-coupling (PCC) voltage $v_{pcc,x}$, and the load current $i_{l,x}$. The continuous-time state-space model is expressed as

$$\dot{\boldsymbol{x}} = \boldsymbol{A}_p \boldsymbol{x} + \boldsymbol{B}_p \boldsymbol{u} + \boldsymbol{F}_p \boldsymbol{v}, \tag{23}$$

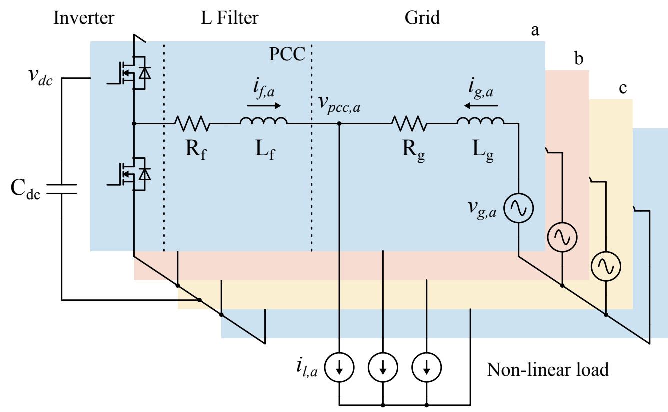

Figure 1. Three-phase four-wire inverter connected to the grid through an L-type filter.

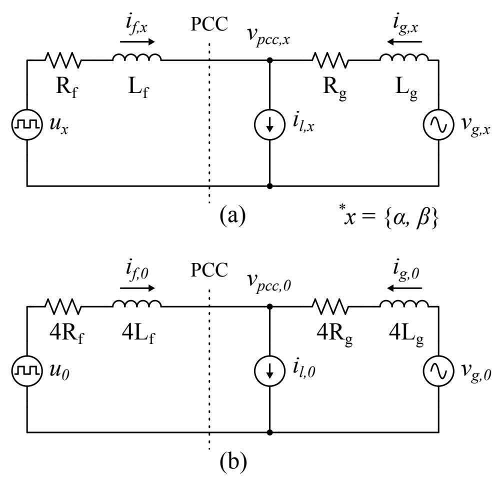

Figure 2. Equivalent plant model in $\alpha\beta0$ coordinates: (a) equivalent circuit for the α or β axis; and (b) equivalent circuit for the 0 axis.

where the state $\boldsymbol{x}$, control $\boldsymbol{u}$, and disturbance $\boldsymbol{v}$ vectors are defined as:

$$\boldsymbol{x} = \begin{bmatrix} i_{f,\alpha} \\ i_{f,\beta} \\ i_{f,0} \end{bmatrix}, \qquad \boldsymbol{u} = \begin{bmatrix} u_\alpha \\ u_\beta \\ u_0 \end{bmatrix}, \qquad \boldsymbol{v} = \begin{bmatrix} v_\alpha \\ v_\beta \\ v_0 \end{bmatrix}. \tag{24}$$

The parameter matrices $\boldsymbol{A}_p$, $\boldsymbol{B}_p$, and $\boldsymbol{F}_p$ are given by:

$$\begin{aligned} \boldsymbol{A}_p &= \operatorname{diag}\left(-\frac{R_f}{L_f}, -\frac{R_f}{L_f}, -\frac{4R_f}{4L_f}\right), \\ \boldsymbol{B}_p &= \operatorname{diag}\left(\frac{1}{L_f}, \frac{1}{L_f}, \frac{1}{4L_f}\right), \\ \boldsymbol{F}_p &= -\boldsymbol{B}_p. \end{aligned} \tag{25}$$

The discrete-time model is derived via the zero-order hold (ZOH) method with sampling period T_s, yielding

$$\boldsymbol{x}_{k+1} = \boldsymbol{A}_d \boldsymbol{x}_k + \boldsymbol{B}_d \boldsymbol{u}_k + \boldsymbol{F}_d \boldsymbol{v}_k, \tag{26}$$

where

$$\begin{aligned} \boldsymbol{A}_d &= e^{\boldsymbol{A}_p T_s}, \\ \boldsymbol{B}_d &= (\boldsymbol{A}_d - \boldsymbol{I})\boldsymbol{A}_p^{-1}\boldsymbol{B}_p, \\ \boldsymbol{F}_d &= (\boldsymbol{A}_d - \boldsymbol{I})\boldsymbol{A}_p^{-1}\boldsymbol{F}_p. \end{aligned} \tag{27}$$

To account for computational delay, the state-space is augmented with delay states ϕ, resulting in the discrete-time system

$$\boldsymbol{z}_{k+1} = \boldsymbol{A}\boldsymbol{z}_k + \boldsymbol{B}\boldsymbol{u}_k + \boldsymbol{F}\boldsymbol{v}_k, \tag{28}$$

with the augmented state $\boldsymbol{z}$ and system matrices defined as:

$$\boldsymbol{z} = \begin{bmatrix} \boldsymbol{x} \\ \boldsymbol{\phi} \end{bmatrix}, \quad \boldsymbol{A} = \begin{bmatrix} \boldsymbol{A}_d & \boldsymbol{B}_d \\ \boldsymbol{0} & \boldsymbol{0} \end{bmatrix}, \quad \boldsymbol{B} = \begin{bmatrix} \boldsymbol{0} \\ \boldsymbol{I} \end{bmatrix}, \quad \boldsymbol{F} = \begin{bmatrix} \boldsymbol{F}_d \\ \boldsymbol{0} \end{bmatrix}. \tag{29}$$

The multivariable system output, corresponding to the filter currents, is given by

$$\boldsymbol{y}_k = \boldsymbol{C}\boldsymbol{z}_k, \quad \boldsymbol{C} = \begin{bmatrix} \boldsymbol{I}_{3\times 3} & \boldsymbol{0}_{3\times 3} \end{bmatrix}. \tag{30}$$

B. Control

Let $i_{l,x}$ denote the load current along axis $x \in \{\alpha, \beta, 0\}$. Applying Kirchhoff's current law at the PCC yields

$$i_{l,x} = i_{g,x} + i_{f,x}, \tag{31}$$

where $i_{g,x}$ is the grid current and $i_{f,x}$ is the filter current regulated by the closed-loop synthesized voltage $\boldsymbol{u}$.

The load powers expressed in the $\alpha\beta 0$ coordinates can be written as

$$\begin{bmatrix} p \\ q \\ p_0 \end{bmatrix} = \begin{bmatrix} v_{pcc,\alpha} & v_{pcc,\beta} & 0 \\ v_{pcc,\beta} & -v_{pcc,\alpha} & 0 \\ 0 & 0 & v_{pcc,0} \end{bmatrix} \begin{bmatrix} i_{l,\alpha} \\ i_{l,\beta} \\ i_{l,0} \end{bmatrix}, \tag{32}$$

where $v_{pcc,x}$ denotes the voltage measured at the converter PCC.

Under harmonic distortion or unbalanced operating conditions, the power terms defined in (32) can be decomposed into average and oscillatory components, given by

$$p = \overline{p} + \tilde{p}, \quad q = \overline{q} + \tilde{q}, \quad p_0 = \overline{p}_0 + \tilde{p}_0, \tag{33}$$

where the superscripts $^-$ and $^\sim$ denote the average and oscillatory components of each power term, respectively.

Based on this power representation, the control objective of the converter is to compensate: (i) the oscillatory active power $\tilde{p}$, (ii) the imaginary power q, and (iii) the zero-sequence power p_0. Achieving this objective ensures that the grid current $i_{g,x}$ supplies only constant active power $\overline{p}$. Consequently, $i_{g,x}$ contains only the fundamental-frequency component and remains in phase with the corresponding voltage in each axis.

To implement this functionality, the control system depicted in the block diagram of Figure 3 is adopted. The diagram is organized into three main blocks: (i) reference current generation, (ii) DC-link voltage control, and (iii) current control.

The reference generation block is based on the p-q theory and employs a Kalman filter and a positive-sequence extraction method to process the PCC voltages, resulting in the reference currents $i^*_{f,\alpha}$, $i^*_{f,\beta}$, and $i^*_{f,0}$ according to the compensation objectives.

The DC-link voltage control aims to regulate the capacitor voltage v_{dc} within prescribed limits. This loop operates indirectly by injecting a power component into the reference generation block and is implemented using an adaptive PID controller. The current control strategy adopted in this work is discussed in the following subsection.

1) Current Control:

The current control loop is implemented using the SVM^{2}PC strategy, which is particularly well-suited for SAPF applications. This approach is particularly suitable for SAPFs, as it enables accurate tracking of reference currents with wide spectral content without requiring multiple controllers tuned to specific harmonic frequencies. Instead, the closed-loop performance is primarily determined by the sampling period.

Based on the augmented plant model defined in (28) and considering a prediction horizon of $N = 3$, the optimization objective is to minimize the squared tracking error of the filter currents in the $\alpha\beta 0$ frame at instant $k+3$:

$$f = \left\| \boldsymbol{i}^*_{f,k+3} - \boldsymbol{i}_{f,k+3} \right\|^2. \tag{34}$$

Given the high harmonic content of the reference current vector, its precise prediction across the horizon is non-trivial. Consequently, a constant reference assumption is adopted over the prediction interval, expressed as

$$\boldsymbol{i}^*_{f,k+3} \approx \boldsymbol{i}^*_{f,k}. \tag{35}$$

This approximation introduces a phase lag proportional to the sampling period T_s, which becomes negligible at high sampling frequencies relative to the fundamental and low-order harmonic components.

Under these assumptions, the unconstrained optimal control action is given by

$$\boldsymbol{u}^*_{uc} = -\left(\boldsymbol{H}^T\boldsymbol{H}\right)^{-1}\boldsymbol{H}^T\boldsymbol{h}, \tag{36}$$

where

$$\begin{aligned} \boldsymbol{H} &= -\boldsymbol{C}(\boldsymbol{A}^2 + \boldsymbol{A} + \boldsymbol{I})\boldsymbol{B}, \\ \boldsymbol{h} &= \boldsymbol{r}_{k+3} - \boldsymbol{C}\boldsymbol{A}^2\boldsymbol{z}_k - \boldsymbol{C}\bar{\boldsymbol{F}}\bar{\boldsymbol{\omega}}_k, \\ \bar{\boldsymbol{F}} &= \begin{bmatrix} \boldsymbol{A}^2\boldsymbol{F} & \boldsymbol{A}\boldsymbol{F} & \boldsymbol{F} \end{bmatrix}. \end{aligned} \tag{37}$$

To reduce computational complexity, the disturbance vector over the prediction horizon is approximated by delayed estimates obtained from the Kalman filter,

$$\bar{\boldsymbol{\omega}}_k = \begin{bmatrix} \hat{\boldsymbol{v}}^T_{f,k-2} & \hat{\boldsymbol{v}}^T_{f,k-1} & \hat{\boldsymbol{v}}^T_{f,k} \end{bmatrix}^T. \tag{38}$$

Since the sampling frequency is considerably higher than the grid frequency, the introduced phase lag remains minimal and exerts a negligible influence on the control performance within the fundamental and low-order harmonic frequency ranges.

C. Results

The performance of the proposed SAPF strategy was validated through a HIL setup utilizing the Typhoon HIL 402 platform and the Typhoon HIL Control Center software. The real-time emulation of the electrical plant was executed with a 0.75 µs sampling step and gate drive oversampling enabled to ensure high-fidelity switching transitions. The control algorithms were implemented in C, with a multirate execution scheme: the high-bandwidth current loop based on SVM^{2}PC operates at 25 kHz, while the outer loops responsible for reference generation and DC-link voltage regulation operate at 12.5 kHz. The key electrical and control parameters adopted in this study are summarized in Table I.

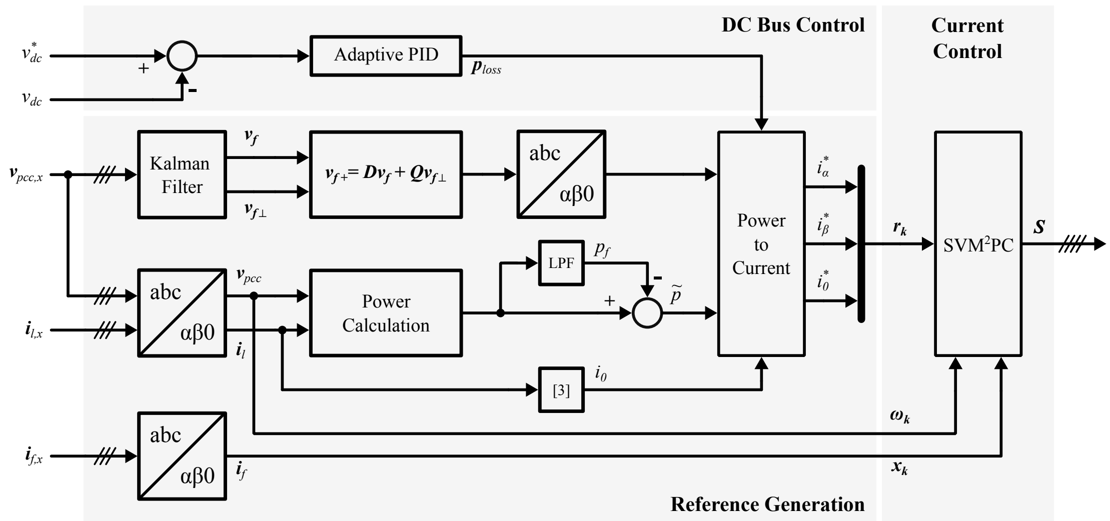

Figure 3. General block diagram of the SAPF.

Table I
SYSTEM AND CONTROL PARAMETERS

Parameter	Symbol	Value
Inverter		
Filter resistance	R_f	0.01 Ω
Filter inductance	L_f	5 mH
DC-link capacitance	C_{dc}	4400 μF
DC-link reference voltage	v_{dc}^*	1000 V
Switching frequency	f_{sw}	25 kHz
Dead-time	t_d	0.1 μs
Grid		
Grid line resistance	R_g	0.2153 Ω
Grid line inductance	L_g	0.285 mH
Current Control		
Sampling frequency	f_s	25 kHz
Prediction horizon	N	3

In this scenario, the performance of the control system is evaluated under an unbalanced load combined with the current drawn by a three-phase rectifier. At instant T_1, the SAPF is connected to the system but draws only the current required for DC-link voltage regulation, becoming fully active at instant T_2. Figure 4 presents the results obtained using the SVM^{2}PC technique.

Figure 4(a) shows the reference and measured currents, highlighting a fast transient response, absence of overshoot, and high tracking capability, even for signals with high rates of variation. Figure 4(b) presents the reference and measured DC-link voltages, indicating that the controlled variable remains close to its reference value, with oscillations below 0.5% of the nominal DC-link voltage.

Figure 4(c) depicts the active, imaginary, and zero-sequence powers supplied by the grid. After SAPF activation at T_2, the amplitude of power oscillations is attenuated, resulting in a less oscillatory behavior. Nevertheless, a small residual noise remains due to the nonlinear current drawn by the three-phase rectifier.

Finally, Figure 4(d) shows the grid currents, where a marked improvement is observed after instant T_2, characterized by a significant reduction in harmonic content, phase current balancing, and, consequently, neutral current cancellation. The harmonic distortion is imposed by a three-phase rectifier connected to the load, which is responsible for generating the nonlinear currents. Small disturbances are observed at the instant when the rectifier starts conducting. Since the approximation $\boldsymbol{r}_k \approx \boldsymbol{r}_{k+3}$ is adopted, these effects cannot be fully compensated due to the phase delay introduced by the prediction.

1) Comparison: The proposed SVM^{2}PC strategy is benchmarked against an FCS-MPC variant based on the same cost function. Although both controllers aim to minimize tracking error, they differ fundamentally in their optimization framework: FCS-MPC employs an exhaustive search of all possible switching vectors over the prediction horizon to select the optimal switching state, which inherently results in a variable switching frequency.

The tracking performance is quantified using classical integral error indices: IAE, ISE, ITAE, and ITSE. The SVM^{2}PC achieved index values of 0.05679, 0.14365, 0.00346, and 0.00779, respectively. In contrast, the FCS-MPC resulted in higher errors across all metrics, with values of 0.11524, 0.31611, 0.00598, and 0.01558, respectively. These results demonstrate that SVM^{2}PC consistently outperforms the conventional predictive approach in both accumulated and time-weighted error categories.

To quantify the performance gain, the percentage error reduction is defined as:

$$E_r = \frac{M_{\mathrm{FCS}} - M_{\mathrm{SVM^2PC}}}{M_{\mathrm{FCS}}} \times 100\%, \tag{39}$$

where M denotes a generic performance metric. Higher E_r values indicate a more substantial improvement of SVM^{2}PC over the FCS-MPC benchmark. Based on this definition, the obtained reductions for IAE, ISE, ITAE, and ITSE were 50.72%, 54.56%, 42.13%, and 50.03%, respectively.

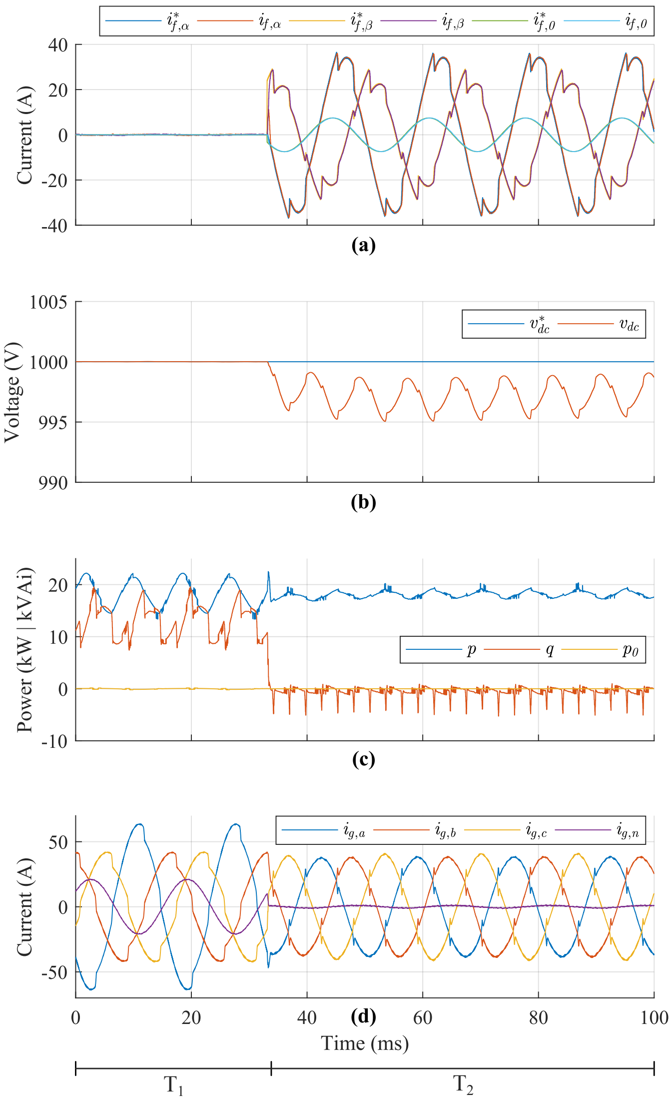

Figure 4. Compensation in the presence of harmonics using SVM^{2}PC: (a) reference and measured active filter currents; (b) reference and measured DC-link voltage; (c) active, imaginary, and zero-sequence powers supplied by the grid; (d) grid currents.

Furthermore, the Total Harmonic Distortion (THD) of the grid current was evaluated up to the 49th harmonic order. Without SAPF compensation, the grid current exhibited a THD of 6.82%. Upon activation of the filters, the THD was reduced to 4.87% using FCS-MPC, and further minimized to 4.83% with the proposed SVM^{2}PC strategy, validating the superior precision of the analytical optimization.

Furthermore, the Total Harmonic Distortion (THD) of the grid current was evaluated up to the 49th harmonic order. Without SAPF compensation, the grid current exhibited a THD of 6.82%. Upon activation of the filters, the THD was reduced to 4.87% using FCS-MPC and to 4.83% with the proposed SVM^{2}PC strategy. Although the improvement over the FCS-MPC benchmark is marginal in terms of harmonic content, the results validate the high precision and effectiveness of the SVM^{2}PC technique.

V. Conclusion

This paper presented the extension of the SVM^{2}PC strategy to three-phase four-wire two-level inverters. The optimization problem was formulated to account for the specific constraints of the four-wire system, and an analytical two-step solution based on KKT conditions was derived to ensure real-time feasibility. HIL validation confirmed precise current tracking, harmonic compensation, and neutral current suppression alongside stable DC-link regulation. Comparative analysis revealed that SVM^{2}PC outperforms FCS-MPC in accumulated error indices while achieving a marginal improvement in total harmonic distortion.

Ongoing research focuses on the implementation of the control algorithm in a digital signal processor to enable Controller-HIL testing and experimental validation in a laboratory-scale microgrid. Additionally, alternative numerical methods for solving the constrained optimization problem are being explored to further reduce the KKT computational burden.

VI. Acknowledgments

This work was supported by CNPq (grants 308082/2025-7, 316436/2021-6) and CAPES/PROEX (Finance Code 001).

References

[1] A. Mora, F. Leiva, R. Cardenas, F. Rojas, J. Pereda, R. P. Aguilera, and J. C. Travieso-Torres, "Optimal switching sequence mpc for four-leg two-level grid-connected converters," *IEEE Journal of Emerging and Selected Topics in Power Electronics*, vol. 12, no. 2, pp. 1271–1281, 2024.

[2] K. Antoniewicz, M. Jasiński, and M. P. Kaźmierkowski, "Model predictive control of three-level four-leg flying capacitor converter operating as shunt active power filter," in *2015 IEEE International Conference on Industrial Technology (ICIT)*, 2015, pp. 2288–2294.

[3] S. C. Ferreira, R. B. Gonzatti, R. R. Pereira, C. H. da Silva, L. E. B. da Silva, and G. Lambert-Torres, "Finite control set model predictive control for dynamic reactive power compensation with hybrid active power filters," *IEEE Transactions on Industrial Electronics*, vol. 65, no. 3, pp. 2608–2617, 2018.

[4] D. H. Chrischon, R. F. De Camargo, G. M. Cocco, and C. A. De Souza, "Finite-set model predictive control and p-q theory applied on shunt active filter in an off-grid microgeneration system," in *2023 15th Seminar on Power Electronics and Control (SEPOC)*, 2023, pp. 1–6.

[5] I. Araujo-Vargas, S. Salas-Duarte, J. Ramirez-Hernandez, B. Del-Muro-Cuellar, and M. Rivera, "Predictive current control of a four-wire, active power filter for an unbalanced utility load of metro railway," in *2015 IEEE International Symposium on Predictive Control of Electrical Drives and Power Electronics (PRECEDE)*, 2015, pp. 79–84.

[6] A. Renault, J. Rodas, L. Comparatore, J. Pacher, and R. Gregor, "Modulated predictive current control technique for a three-phase four-wire active power filter based on h-bridge two-level converter," in *2018 53rd International Universities Power Engineering Conference (UPEC)*, 2018, pp. 1–6.

[7] A. Renault, M. Riveray, L. Comparatore, J. Pacher, J. Rodas, and R. Gregor, "Model predictive current control with neutral current elimination for h-bridge two-level active power filters," in *2016 IEEE Ecuador Technical Chapters Meeting (ETCM)*, 2016, pp. 1–5.

[8] T. Martins Bezerra, N. Rocha, A. De Medeiros Maciel, E. Luiz Lopes Fabrício, and K. Bezerra De Carvalho, "Predictive control applied to three-phase four-wire shunt active power filters: An innovative approach," in *2023 IEEE 8th Southern Power Electronics Conference and 17th Brazilian Power Electronics Conference (SPEC/COBEP)*, 2023, pp. 1–7.

[9] D. Schuetz, C. R. D. Osório, L. A. Maccari, D. M. Lima, F. d. M. Carnielutti, V. F. Montagner, and H. Pinheiro, "Space vector modulated model predictive control for grid-tied converters," *IEEE Transactions on Industrial Informatics*, vol. 19, no. 1, pp. 414–425, 2023.